

Frequency-domain calculation of Smith-Purcell radiation for metallic and dielectric gratings

ANDRZEJ SZCZEPKOWICZ,¹ LEVI SCHÄCHTER,² JOEL ENGLAND³

¹*Institute of Experimental Physics, University of Wrocław, Plac M. Borna 9, 50-204 Wrocław, Poland*

²*Technion–Israel Institute of Technology, Haifa 32000, Israel*

³*SLAC National Accelerator Laboratory, 2575 Sand Hill Road, Menlo Park, CA 94025, USA*

Abstract: The intensity of Smith-Purcell radiation from metallic and dielectric gratings (silicon, silica) is compared in a frequency-domain simulation. The numerical model is discussed and verified with the Frank-Tamm formula for Cherenkov radiation. For 30 keV electrons, rectangular dielectric gratings are less efficient than their metallic counterpart, by an order of magnitude for silicon, and two orders of magnitude for silica. For all gratings studied, radiation intensity oscillates with grating tooth height due to electromagnetic resonances in the grating. 3D and 2D numerical models are compared.

© 2020 Optical Society of America

1. Introduction

The Smith-Purcell (SP) radiation, observed for visible light in 1953 [1], has been shown to occur in a wide spectral region, from microwaves [2,3] generated using macroscopic gratings, to ultraviolet radiation [4, 5] from nanogratings. One foreseen application of this effect would be a highly tunable free-electron light source [6]. SP radiation might also be used for beam diagnostics in accelerators, for beam position monitoring [7–9] or longitudinal profile characterization [10–14]. New motivation to study SP radiation comes from the development of Dielectric Laser Accelerators (DLA) [15, 16], which utilize the inverse Smith-Purcell effect. Electron beams from DLA may in turn be used to generate SP radiation in various spectral regions.

The majority of experimental studies of SP radiation were carried out with metallic gratings. Some recent studies deal with dielectric gratings (eg. [6, 17]); this is caused by advances in dielectric nanofabrication, improved understanding of SP emission from dielectrics, and hope that dielectrics may in some cases outperform metals in radiation intensity [6].

Calculations of SP radiation intensity from gratings have a long history. Most analytical work to date considers only metallic gratings (exception: a very simplified model in Ref. [18] applied to sub-THz radiation). Ref. [19] reviews some of the analytical models, and their outcomes are compared in Refs [20, 21]. Many of the models build upon the seminal work by Toraldo di Francia [22], which treats both SP and Cherenkov radiation with the same formalism (“Cherenkovian effects”). The range of analytical methods include perturbative approaches valid for shallow gratings [23, 24] and various surface current models [19, 25–28] which are best suited for shallow gratings, but for high energies can also be applied to deep profiles [25]. Most of the analytical models involve some approximations and neglect resonant cavity effects in the grating. According to Ref. [20] the results of different analytical models may differ by up to six orders of magnitude. An exceptional position among the analytical models of SP radiation is held by the van den Berg’s model [29–31]. According to the author the model is rigorous and is applicable to arbitrary grating profile. Although the model’s accuracy has been questioned [25], no one has explicitly shown the model to be inexact. The model does reproduce radiation intensity

oscillations with increasing tooth height [32], a resonant cavity effect in the grating. However, van den Berg’s approach is probably the most difficult of the SP models to apply and in the end requires nontrivial numerical calculations [25, 29, 33].

Metals are easier to deal with in analytical models than dielectrics, because with the perfect electric conductor boundary condition it is not necessary to solve for the field inside and on the other side of the grating. Regarding dielectric gratings, Sukhikh et al. [18] report analytical calculation of SP radiation from a teflon grating, however with several special assumptions: geometry of an inverted lamellar grating (rectangular grating) with substrate thickness approaching zero, SP radiation only to one side, and neglect of secondary refractions (resonances within the grating are not reproduced); the model has been applied in [18] for sub-THz radiation.

In recent years an increasing number of purely numerical simulations of SP radiation were reported. Numerical simulations are equally applicable to metallic and dielectric gratings, although for a dielectric grating more time and memory resources are needed. The most common approach is a time-domain simulation; some recently used solvers are Lumerical FDTD [34–37] and CST [38–41]. The time of calculation is usually from hours to days on a single CPU machine. Another approach is a frequency-domain simulation, which is much faster if infinite gratings are assumed (simulation for one unit cell with periodic boundary conditions). This approach was used in Refs. [17, 37, 42]; however, none of these papers describes the method of simulation, and it is hard to deduce how radiation energy was calculated. A description of the simulation method can be found in papers which report frequency-domain calculations of Cherenkov radiation [43–45], but these papers do not compute radiated energy. All of the Refs. [17, 37, 42–45] use the Comsol frequency-domain solver [46].

The present work focuses on frequency-domain simulation of single-electron (“incoherent”) Smith-Purcell radiation with metallic and dielectric gratings. We start in Sect. 2 with a step-by-step description of calculation method for Smith-Purcell and Cherenkov radiation (“Cherenkovian effects” [22]) using a frequency-domain numerical solver. Although simple in principle, the solution requires careful differentiation between phasors (as required by the numerical solver) and phasor densities (Fourier transforms) and proper interpretation of the well known expression $\text{Re}[\frac{1}{2}\mathbf{E} \times \mathbf{H}^*]$, which is different for phasors and for phasor densities. Careful treatment leads to the solution that is correct in absolute terms, without spurious multiplicative constants. We verify our method by comparing the results for Cherenkov radiation with the exact analytical Frank–Tamm formula for radiated energy [47–49].

After the detailed deliberations on methodology we turn to applications. In Sect. 3 we use our frequency-domain model to compare directly radiation from gratings of fixed geometry and different materials, which to our knowledge has not yet been reported in the literature, except for the mentioned previously very limited model in Ref. [18], and except for a recent paper [6], which however compares theoretical upper bounds for SP radiation, not the actual computed values. In Sect. 4 we demonstrate that the model captures resonant effects in the grating. While energy oscillations with increasing tooth height have been reported previously for metallic gratings [32, 38, 39, 50], we demonstrate them for the first time for dielectrics. Section 5 briefly compares a numerical result from a three-dimensional (3D) and a two-dimensional (2D) model. This is an important issue, as the 3D models require large RAM memory and are more difficult to construct, so one usually starts with 2D modelling. Section 6 briefly describes radiation from triangular gratings, and Sect. 7 summarizes the paper.

In all equations in this paper we use SI units.

2. Calculation of Smith-Purcell or Cherenkov radiation intensity with a frequency-domain solver

2.1. Phasors vs. phasor densities and the expression for energy

To perform calculations using a numerical frequency-domain solver, we must carefully distinguish between phasors and phasor densities. In case of time-harmonic electromagnetic field we have

$$\mathbf{J}(\mathbf{r}, t) = \text{Re}[\mathbf{J}(\mathbf{r})e^{j\omega_0 t}] = \frac{1}{2}[\mathbf{J}(\mathbf{r})e^{j\omega_0 t} + \mathbf{J}^*(\mathbf{r})e^{-j\omega_0 t}] \quad (1a)$$

$$\mathbf{E}(\mathbf{r}, t) = \text{Re}[\mathbf{E}(\mathbf{r})e^{j\omega_0 t}] = \frac{1}{2}[\mathbf{E}(\mathbf{r})e^{j\omega_0 t} + \mathbf{E}^*(\mathbf{r})e^{-j\omega_0 t}] \quad (1b)$$

and similarly for the \mathbf{B} , \mathbf{D} and \mathbf{H} fields. The phasors, denoted here $\mathbf{J}(\mathbf{r})$, $\mathbf{E}(\mathbf{r}) \dots$, are distinct from the temporal Fourier transforms (phasor spectral densities) $\mathbf{J}(\mathbf{r}, \omega)$, $\mathbf{E}(\mathbf{r}, \omega)$, \dots :

$$\begin{aligned} \mathbf{J}(\mathbf{r}, t) &= \frac{1}{2}[\mathbf{J}(\mathbf{r})e^{j\omega_0 t} + \mathbf{J}^*(\mathbf{r})e^{-j\omega_0 t}] = \int_{-\infty}^{\infty} e^{j\omega t} \mathbf{J}(\mathbf{r}, \omega) d\omega \\ &= \int_{-\infty}^{\infty} e^{j\omega t} \left\{ \frac{1}{2}[\mathbf{J}(\mathbf{r})\delta(\omega - \omega_0) + \mathbf{J}^*(\mathbf{r})\delta(\omega + \omega_0)] \right\} d\omega \end{aligned} \quad (2)$$

where we use a Fourier transform convention consistent with [51, 52]. Equation (2) implies that for time-harmonic fields, the Fourier transforms can be expressed in terms of the corresponding phasors as

$$\mathbf{J}(\mathbf{r}, \omega) = \frac{1}{2}[\mathbf{J}(\mathbf{r})\delta(\omega - \omega_0) + \mathbf{J}^*(\mathbf{r})\delta(\omega + \omega_0)] \quad (3a)$$

$$\mathbf{E}(\mathbf{r}, \omega) = \frac{1}{2}[\mathbf{E}(\mathbf{r})\delta(\omega - \omega_0) + \mathbf{E}^*(\mathbf{r})\delta(\omega + \omega_0)], \text{ etc.} \quad (3b)$$

Note the difference in units: $\mathbf{J}(\mathbf{r}, \omega)$ [$\text{s} \cdot (\text{A}/\text{m}^2)$], $\mathbf{J}(\mathbf{r})$ [A/m^2], etc.

Maxwell equations in the frequency domain („time-harmonic”)

$$\nabla \times \mathbf{E} + j\omega \mathbf{B} = 0 \quad (4a)$$

$$\nabla \times \mathbf{H} - j\omega \mathbf{D} = \mathbf{J} \quad (4b)$$

$$\nabla \cdot \mathbf{D} = \rho \quad (4c)$$

$$\nabla \cdot \mathbf{B} = 0 \quad (4d)$$

are valid both for phasors and for temporal Fourier transforms, and this may lead to confusion about the meaning of symbols \mathbf{J} , \mathbf{E} , \dots in a particular context. A frequency-domain solver in engineering-oriented software like Comsol expects a phasor expression for electric current $I(\mathbf{r})$ [A] (or current density $\mathbf{J}(\mathbf{r})$ [A/m^2]), and outputs phasors $\mathbf{E}(\mathbf{r})$ [V/m] and $\mathbf{B}(\mathbf{r})$ [T]. The total energy radiated through a surface is

$$W = \int_{-\infty}^{\infty} \int_{\text{surface}} \text{Re} \left[\frac{1}{2} \mathbf{E}(\mathbf{r}) \times \mathbf{H}^*(\mathbf{r}) \right] \cdot d\mathbf{A} dt \quad (5)$$

where $\frac{1}{2} \mathbf{E} \times \mathbf{H}^*$ is the complex Poynting vector [52] and $\text{Re}[\frac{1}{2} \mathbf{E} \times \mathbf{H}^*]$ is the time-averaged power flux density (PFD) [W/m^2] (in Comsol it is called “Power flow, time average, Poav ”). Note that for strictly harmonic fields expression (5) is infinite.

We can “cheat” the solver by entering a temporal Fourier transform for current $I(\mathbf{r}, \omega)$ instead of a phasor $I(\mathbf{r})$, then the solver will use the same equations (4) as for phasors to calculate the Fourier transforms $\mathbf{E}(\mathbf{r}, \omega)$, $\mathbf{B}(\mathbf{r}, \omega)$, \dots . Now the expression $\text{Re}[\frac{1}{2} \mathbf{E} \times \mathbf{H}^*]$ has a different

interpretation and a different unit [$\text{s}^2 \cdot \text{W}/\text{m}^2$]. As shown in Appendix A, the total radiated energy is now equal to

$$W = \int_0^\infty \underbrace{\int_{\text{surface}} 4 \cdot 2\pi \cdot \text{Re} \left[\frac{1}{2} \mathbf{E}(\mathbf{r}, \omega) \times \mathbf{H}^*(\mathbf{r}, \omega) \right] \cdot d\mathbf{A}}_{dW/d\omega} d\omega \quad (6)$$

where $dW/d\omega$ is the radiated energy per unit frequency. Here we use only positive frequencies to allow comparison with experimental results. The numerical factor $4 \cdot 2\pi$ depends on which convention for Fourier transforms is used, here it is consistent with Equations (2), (8), (9). To obtain $dW/d\omega$ from the solver's result, take the surface integral of $\langle \mathbf{PFD} \rangle$ (Comsol: `POAV`) and multiply by $4 \cdot 2\pi$; the result is in [$\text{J} \cdot \text{s}$] (for phasors it would be [J/s]). Depending on the software used, the “cheated” solver may signal wrong units. This can be resolved by multiplying the expression for current by an arbitrary frequency range $\Delta\omega$, for example by unit angular frequency $\Delta\omega = 1$ [$1/\text{s}$] and dividing $\langle \mathbf{PFD} \rangle$ by $(\Delta\omega)^2$.

The expression $\text{Re}[\frac{1}{2}\mathbf{E} \times \mathbf{H}^*]$ is discussed in many electrodynamics texts for phasors $\mathbf{E}(\mathbf{r})$, $\mathbf{H}(\mathbf{r})$, but its interpretation for transforms $\mathbf{E}(\mathbf{r}, \omega)$, $\mathbf{H}(\mathbf{r}, \omega)$ and the formula (6) cannot easily be found in textbooks. To calculate power using a phasor-based frequency-domain code, one needs to compare directly equations (5) and (6). Formulas similar to (6) appear in some papers dealing with analytical models of S-P radiation [24, 53, 54], but may be not evident to users of numerical frequency-domain codes (for example, this issue is not addressed in tutorials and manuals of Comsol [46]). Ref. [55] presents a heuristic argument for energy computation in a frequency domain solver, which however leads to results that are too small by a factor of 4. Adding to confusion, the expression $\text{Re}[\frac{1}{2}\mathbf{E}(\mathbf{r}, \omega) \times \mathbf{H}^*(\mathbf{r}, \omega)]$ is sometimes called “Poynting vector in the frequency domain” [53], which can easily be misunderstood as the Fourier transform of the Poynting vector (these are distinct quantities with different units, see also Appendix A). Another source of confusion is that energy density may be defined on either $\omega \in (-\infty, \infty)$ or $\omega \in (0, \infty)$ – the two definitions differ by factor 2. Incorrect numerical factors can also arise when rivaling Fourier transform conventions from different papers are confused. All these problems call for some verification of calculated radiation intensities. This issue will be addressed in Sect. 2.4.

2.2. Moving point charge – expression for current and Floquet-periodicity

To calculate Smith-Purcell radiation or Cherenkov radiation, we consider a point charge ($-e$) moving in the $\hat{\mathbf{z}}$ direction with constant velocity $v = \beta c$. For a particle at $z = 0$ when $t = 0$ the current density is

$$\mathbf{J}(\mathbf{r}, t) = (-e)v\delta(x)\delta(y)\delta(z - vt)\hat{\mathbf{z}} = (-e)\delta(x)\delta(y)\delta(z/v - t)\hat{\mathbf{z}}. \quad (7)$$

After integration over the transverse coordinates x, y , we obtain the expression for the current

$$\begin{aligned} I(z, t) &= (-e)\delta(z/v - t) = (-e)\frac{1}{2\pi} \int_{-\infty}^{\infty} e^{-j\omega(z/v - t)} d\omega \\ &= \int_{-\infty}^{\infty} \left\{ \frac{(-e)}{2\pi} e^{-j(\omega/v)z} \right\} e^{j\omega t} d\omega, \end{aligned} \quad (8)$$

so the temporal Fourier transform of $I(z, t)$ is

$$I(z, \omega) = \frac{(-e)}{2\pi} e^{-j(\omega/v)z}. \quad (9)$$

This expression is input to the solver as the “edge current”. Note that the current is a function of the longitudinal coordinate and not all of the frequency-domain solvers will allow for this

dependence on position. The current is Floquet-periodic:

$$I(z + a, \omega) = I(z, \omega) \exp(-jk_F a), \quad (10)$$

with the Floquet vector $k_F = \omega/v$. For a uniform or a periodic medium, the same spatial periodicity in the frequency domain is followed by the fields:

$$\mathbf{E}(x, y, z + a, \omega) = \mathbf{E}(x, y, z, \omega) \exp(-jk_F a), \quad (11)$$

$$\mathbf{H}(x, y, z + a, \omega) = \mathbf{H}(x, y, z, \omega) \exp(-jk_F a). \quad (12)$$

For Cherenkov radiation in a uniform medium a is arbitrary. For a non-uniform medium the Floquet periodicity occurs if the refractive index is periodic in z (eg. an infinite grating) – in this case a must be equal to the period. For non-periodic systems (eg. a finite grating) Eqs. (11–12) do not hold. However, they should hold in an approximate sense near the center of a finite structure with many periods.

2.3. Infinite gratings – geometry of the model

In this paper we consider infinite gratings, periodic in the z coordinate. The described model is valid for arbitrary grating profile. We choose to focus on simple grating profiles: rectangular, and in Sect. 6 – triangular. As expected for numerical models, there is no additional difficulty if any other grating profile is considered, as long as the profile is well resolved by the calculation mesh (for 3D models computer memory limits may come into play).

Figure 1 shows the basic grating and beam configuration assumed in this paper. The electric charge moving in the \hat{z} direction at a distance d from a grating is the source of SP radiation. In the 3D model the source is a point charge e , and all radiation at a given frequency ω is collected. The 2D model corresponds to the source being a line charge with charge density $e/\Delta y$, and radiation collected from a corresponding strip of width Δy . In the latter case the resulting radiated energy depends on the arbitrary transverse length Δy – this issue will be addressed in Sect. 5.

Figures 2 and 3 show the details of the model. For infinite gratings only one unit cell is needed in the calculation. The boundaries of the calculation domain in the $\pm\hat{z}$ directions are connected by the Floquet boundary condition (11–12). Perfectly Matched Layers (PMLs) attenuate radiation in the transverse directions. The calculation domain consists of vacuum, characterized by relative permittivity = 1, and the grating region, characterized by arbitrary complex relative permittivity ϵ . Note that “top” PMLs are vacuum, while the “bottom” PMLs are grating material, see Figs. 2(b), 3(b). This means that we model thick gratings (this case occurs more often in the experiments). If the bottom PML is changed to vacuum, a thin grating is modelled, reflections from the back side of the grating occur, and guided mode resonances occur for certain frequencies (see Ref. [56] and references therein), with major impact on the radiation intensity. The 3D model is more realistic than a 2D model, but requires large RAM memory (10–20 GB); the computation time for a single frequency is of the order of minutes on a single CPU machine. The 2D model requires much less memory and the computation time is of the order of seconds. In the 3D simulation, radiation at a given frequency ω is collected from all transverse directions, by calculating the surface integral in Eq. (6) over the inner boundary of the PML (violet cylindrical strip in Fig. 3(a)). In the 2D model, for a given frequency ω , the integration is carried out over the planar inner PML boundary (Fig. 2(b)).

We performed all calculations using the frequency-domain solver in the Comsol simulation software environment [46], which utilizes the Finite Element Method (FEM). The FEM mesh is shown in Fig. 3(d). We tried various refinements of the mesh and obtained slight scatter of the computed results. On the basis of these trials we believe that the numerical values presented in this paper are accurate up to $\pm 20\%$, limited by the used hardware (20 GB RAM). Frequency-domain FEM method can also be applied to ultrarelativistic particles [57], but the mesh has to be refined

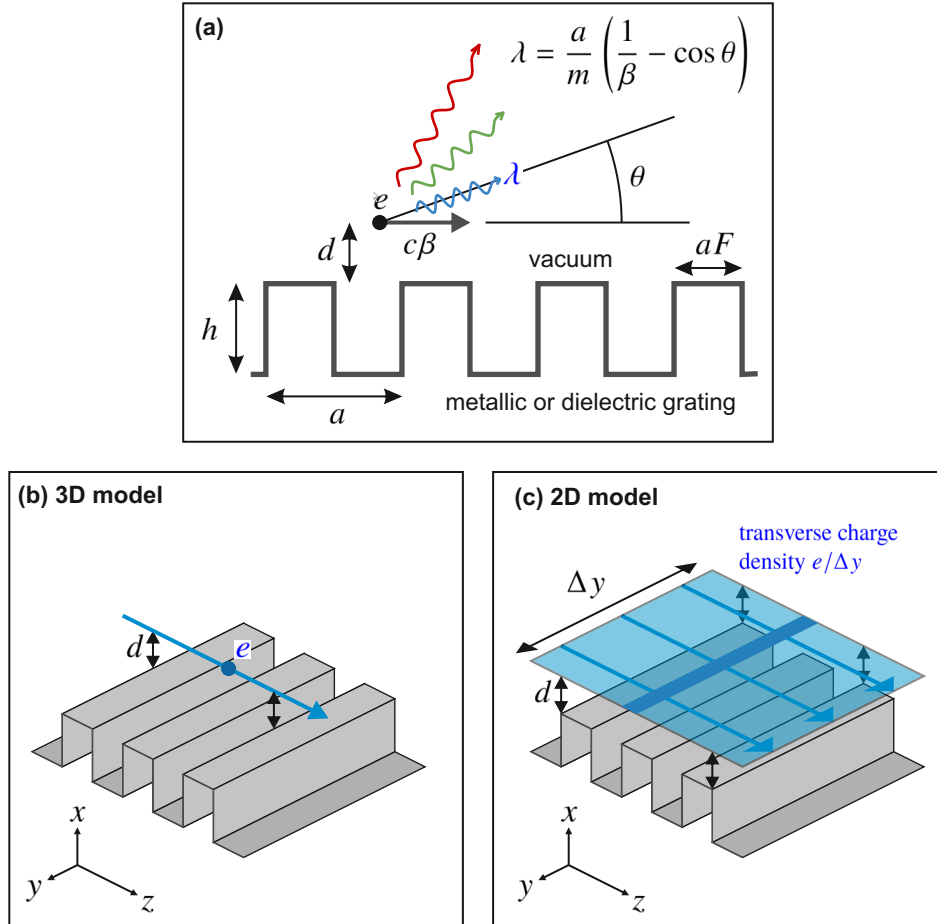


Fig. 1. (a) Basic grating and beam configuration assumed in this paper: grating period $a = 300$ nm, tooth height $h = 200$ nm, fill factor $F = 0.5$, $\beta = 0.328$ corresponding to 30 keV electrons, impact parameter $d = 100$ nm. We focus on the radiation in first spectral order $m = 1$. For $\theta = 90^\circ$ the radiation wavelength is $\lambda_{\perp} = 914$ nm. (b) A 3D model with a moving point charge; the grating is infinite in the y and z directions. (c) A 2D model, invariant in the y direction and infinite in the z direction, with a moving line charge (flat beam pulse).

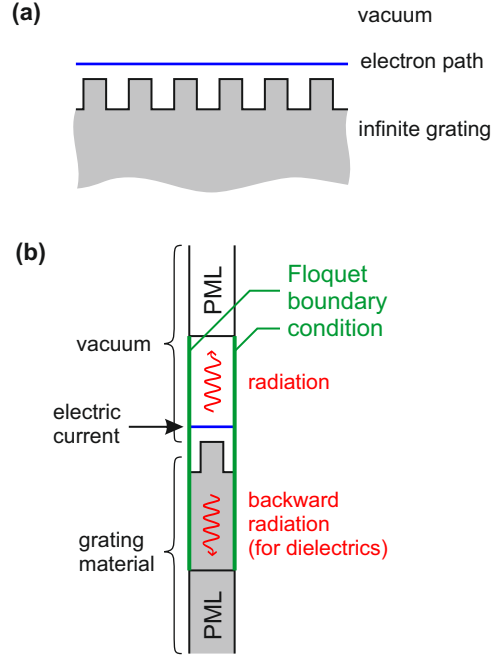


Fig. 2. (a) A 2D infinite grating is modelled as a (b) 2D unit cell with the Floquet boundary conditions.

along z to account for the contraction of the electromagnetic field of the electron. We note one numerical peculiarity: in Comsol, for 3D models, the default iterative solver fails to find a solution within one hour, but if the direct solver is chosen, the solution is found within minutes.

2.4. Verification of the model against the Frank-Tamm formula

At the end of Sect. 2.1 we pointed out several pitfalls that may lead to incorrect multiplicative factors in calculations of SP radiation intensity. This doesn't matter if only relative intensity is needed or one aims at order-of-magnitude estimates, but if accurate results are needed, it is best to initially test the used model against some rigorous analytical result. We propose a novel approach to this problem. We take advantage of the fact that the numerical model described above is the same for SP and for Cherenkov radiation – the only difference is in the distribution of relative permittivity in space, $\epsilon(\mathbf{r})$. So for a moment we change the relative permittivity of the vacuum region to ϵ and calculate the radiated energy in the uniform medium – the Cherenkov radiation, shown in Fig. 4, and compare the radiation intensity with the Frank-Tamm formula, Eq. (31) in Appendix B. The results are shown in Table 1. The ratio of the numerical radiated energy $d^2W_{\text{num}}/dz d\omega$ to the analytical value is close to 1, within 10%. The slight discrepancy can be reduced by refining the FEM mesh (within accessible computer memory). The parameters in the last row in the table do not fulfil the Cherenkov radiation condition (see Appendix B); in this case the calculated energy is 20 orders of magnitude lower, on the level of numerical noise of the calculation – this is the expected result. We also checked that the computed energy is linear in ω . These results demonstrate that our model is exact, with no spurious multiplicative factors.

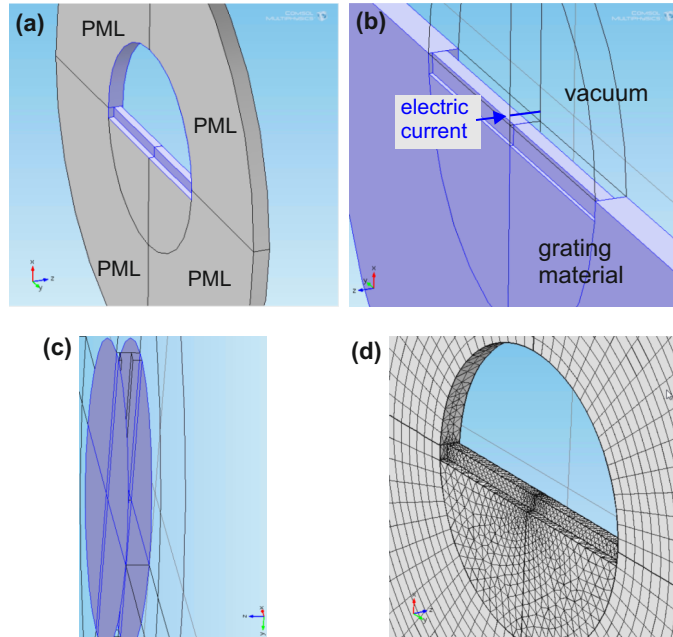


Fig. 3. A 3D infinite grating is modelled as a 3D unit cell with the Floquet boundary conditions. (a) Perfectly matched layers (PMLs). (b) Electron path. (c) A pair of surfaces with Floquet boundary condition. (d) An example mesh used by a finite element method solver (Comsol).

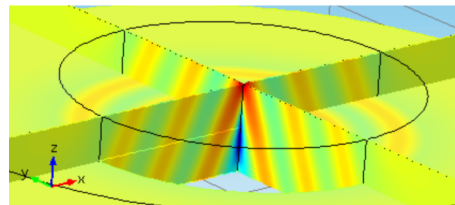


Fig. 4. Cherenkov radiation – visualization of the Fourier transform of the electric field, $\text{Re}[E_z(\mathbf{r}, \omega)]$, for $\omega = 2\pi \cdot 4 \cdot 10^{14} \text{ s}^{-1}$, $\beta = 0.5$, $n = 5$.

Velocity and refractive index	$\frac{d^2W_{\text{num}}}{dz d\omega} / \frac{d^2W_{\text{analytical}}}{dz d\omega}$
$\beta = 0.33, n = 3.6$	1.04
$\beta = 0.5, n = 3.6$	1.08
$\beta = 0.5, n = 5$	1.04
$\beta = 0.3, n = 2$	no radiation

Table 1. Cherenkov radiation – verification of the numerical results against the Frank-Tamm formula for one frequency, $\omega = 2\pi \cdot 4 \cdot 10^{14} \text{ s}^{-1}$. Here we compare the numerical value $d^2W_{\text{num}}/dz d\omega$ against the analytical value $d^2W_{\text{analytical}}/dz d\omega = (e^2/4\pi)\mu_0\omega(1 - 1/\beta^2n^2)$ (see Appendix B); the second column shows the ratio of these two values.

3. Comparison of radiation from metallic and dielectric gratings

We assume grating and beam configuration described in Fig. 1(a–b), a 3D model, and calculate the SP radiation emitted within the frequency range $2\pi \cdot 325.5 \text{ THz} < \omega < 2\pi \cdot 330.5 \text{ THz}$; this corresponds to radiation emitted perpendicular to the grating within 5 THz bandwidth, into angles $88.7^\circ < \theta < 91.3^\circ$; the corresponding wavelength range is $907 \text{ nm} < \lambda < 921 \text{ nm}$; see the SP formula in Fig. 1(a).

To simulate a perfect conductor, we set the relative permittivity to $\epsilon = -10000 + 0i$ – large negative real part and zero imaginary part. This is based on the observation that for optical frequencies good conductors have a large negative real part of ϵ (eg. $\epsilon(\text{Cu}) = -36.8 + 1.36i$, $\epsilon(\text{Au}) = -38.4 + 1.46i$ at $\lambda = 914 \text{ nm}$ [58, 59]), while the imaginary part of ϵ describes energy dissipation and should vanish for a perfect conductor. This corresponds to large imaginary index of refraction $n = 100i$, yielding almost instantaneous decay of the field inside the material (skin depth = $0.0016\lambda = 1.5 \text{ nm}$). We verified numerically that for S–P radiation from metallic gratings in the considered frequency range, the bulk condition $\epsilon = -10000 + 0i$ yields the same result as the surface PEC condition (Perfect Electric Conductor, $\hat{\mathbf{n}} \times \mathbf{E} = \mathbf{0}$); this would not be valid in the sub-THz frequency range [18]. While the boundary condition is computationally more efficient, we choose to use the bulk condition, so that exactly the same numerical model can be applied both to metallic and dielectric gratings – only the grating’s relative permittivity ϵ is changed.

The resulting SP radiation for five materials is shown in Table 2. Metallic gratings outperform dielectric gratings by 1–2 orders of magnitude in terms of radiation intensity under the conditions studied (simple rectangular grating, 30 keV electrons, radiation wavelength $\sim 1 \text{ }\mu\text{m}$). This confirms expectations from comparison of theoretical upper bounds for radiation from Ref. [6] (plot of “material factor” in Supplementary Fig. 10). An interesting observation is that for dielectric gratings twice more energy is radiated inside the grating than emitted as external SP radiation. It is an interesting question whether the energy radiated inside could be reflected using eg. a vacuum/dielectric Bragg mirror (DBR) [62].

Data in Table 2 is a direct comparison of SP radiation from metallic and dielectric gratings, however it is only for one set of beam and grating parameters. In future work the study should be extended to other electron energies, grating configurations and radiation angles. In particular, it would be interesting to check the prediction from Ref. [6] that silicon may outperform metals for very low energy electrons (below 10 eV).

Grating material	Relative permittivity ($\lambda = 914$ nm)		Radiated energy W	Energy radiated into the grating W_{in}
	Real part ϵ_1	Imaginary part ϵ_2		
Copper	-36.85	1.361	$4.4 \cdot 10^{-25}$ J	0
Gold	-38.36	1.462	$4.4 \cdot 10^{-25}$ J	0
Perfect conductor	-10000	0	$3.1 \cdot 10^{-25}$ J	0
Fused silica	2.107	0	$4.8 \cdot 10^{-27}$ J	$8.8 \cdot 10^{-27}$ J
Silicon	13.32	0.03099	$3.0 \cdot 10^{-26}$ J	$6.8 \cdot 10^{-26}$ J

Table 2. SP radiation from gratings of different materials, emitted perpendicular to the grating within the frequency range $2\pi \cdot 325.5$ THz $< \omega < 2\pi \cdot 330.5$ THz, corresponding to angular range $88.7^\circ < \theta < 91.3^\circ$, per electron per grating period, for the grating geometry and beam parameters from Fig. 1(a-b). Relative permittivity is taken from Refs. [58–61].

4. Energy oscillations with grating tooth height – grating resonances

Results of the previous section were for a grating with a fixed tooth height. Does the intensity of SP radiation change if the tooth height is changed? The answer is shown in Fig. 5. SP radiation intensity W oscillates with increasing tooth height h (the impact parameter d is kept constant, see Fig. 1). The effect is known for metallic gratings, it has been experimentally observed in the millimeter-wave spectral region using a special metallic grating setup with variable tooth height [32]. The effect has also been shown for metallic gratings in an analytical calculation based on van den Berg’s model [32] and in numerical time-domain models [32, 38, 39, 50]. Here we confirm oscillations of $W(h)$ for metallic gratings in a frequency-domain simulation; in addition, we demonstrate that the oscillations also occur for dielectric gratings, see Fig. 5(b–c). An interesting result is that for all materials, the optimum tooth height is close to one quarter of the radiation wavelength in the perpendicular direction.

The $W(h)$ oscillations are of resonant nature. Similar effects for the more general phenomenon of diffraction radiation [63] have been predicted for the motion of charged particles near an open metallic or dielectric resonator [64, 65] or an array of metallic resonators [66]; enhanced radiation occurs for frequencies close to one of the resonant frequencies of the cavity. In case of the oscillatory effect shown in Fig. 5, the cavity is formed between adjacent grating teeth. The essence of the effect is already captured by a 2D model, see Fig. 6. The green insets show the analogy with the elementary one-dimensional theory of clarinets or organ pipes, where the resonant lengths of a cavity which is open at one end, for a fixed wavelength λ , are equal to $\frac{1}{4}\lambda + m \cdot \frac{1}{2}\lambda$ (vertical dashed lines in Fig. 6; see also Ref. [38]). This simple one-dimensional reasoning explains the essence of the effect, but does not explain the slight shift of the calculated radiation maxima $W(h)$ towards smaller h . Note that in the acoustic case this model is also approximate. The simple model does not work in case of dielectric cavities – the period of $W(h)$ oscillations in Fig. 5(b–c) has no obvious relation to the vacuum wavelength or the wavelength inside the dielectric; maybe one could deduce the effective wavelength on the grounds of effective mode index theory.

The intensity oscillations for a metallic grating can alternatively be explained by considering the groove cavity as a transmission line which is short-circuited at one end (bottom of the groove; impedance = 0) and open-circuited at the other end (top of the groove). If in the groove only

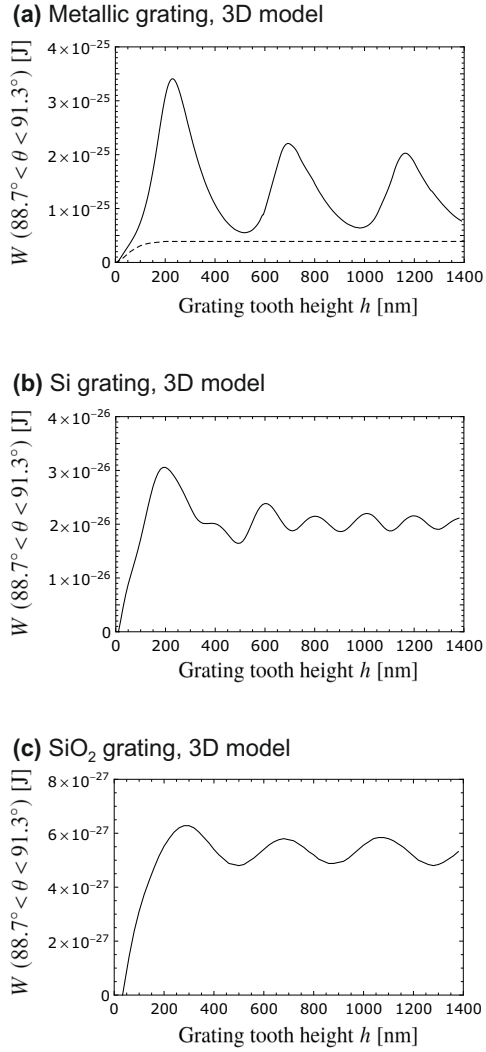


Fig. 5. SP radiation from gratings of different materials, in the angular range $88.7^\circ < \theta < 91.3^\circ$, per electron per grating period, for grating geometry shown in Fig. 1(a–b) (3D model). Solid line – numerical calculation in the frequency domain. For the metallic grating the result is compared with an analytical calculation based on Ref. [28] – dashed line.

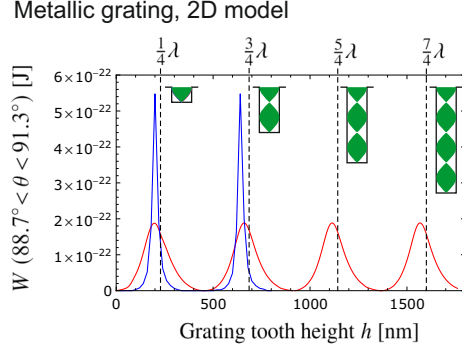


Fig. 6. SP radiation from gratings of different tooth heights h , in the angular range $88.7^\circ < \theta < 91.3^\circ$, per electron per grating period, for grating geometry shown in Fig. 1(a,c) (2D model) with $\Delta y = 1$ nm. Grating fill factor $F = 0.5$ (red) and $F = 0.9$ (blue).

the TEM mode is considered (transmission line approximation), the first resonance will occur when $h = \lambda/4$ (high impedance at the top end of the line). However, in practice many other modes must be used in order to satisfy the boundary conditions. Due to the presence of these evanescent modes electromagnetic energy is stored near the edge (top) of the groove. Effectively, this stored energy is manifested in a shift in frequency (see Fig. 6), since in general near an edge the magnetic energy does not equal the electric energy $\hat{A}\hat{S}$ as is the case in an ideal cavity or plane waves. This effect is well known in waveguide theory and it is usually described in terms of length: the electrical length differs from the geometrical length.

The van den Berg's model cannot be applied to dielectrics, but it would be interesting to compare it with oscillations shown in Fig. 5(a) for metallic grating, similarly as was done in Ref. [32]. However, van den Berg's model is not easy to apply, so instead we compare our numerical results with the analytical results of a surface current model, using expressions from Ref. [28] (dashed line in Fig. 5(a)). An order of magnitude agreement is found, but the surface current model does not predict oscillations of $W(h)$. The explanation can be found in the original paper by Brownell, Walsh and Doucas: "in deep tooth profiles several facets may form a cavity and limit the field modes when the wavelength is comparable to or longer than the cavity dimensions. The model described here is best suited for shallow gratings where cavity behavior is negligible but can be applied to deep profiles if the energy is sufficiently high so that the wavelength is much smaller than any cavity" [25].

5. Comparison of 3D and 2D results for the Smith-Purcell radiation

As was shown in the previous section, certain effects in the SP radiation can be captured well within a 2D model, which is much simpler to construct than a 3D model. What about radiation intensity: can we estimate it from a 2D model? Comparison of the numbers in Figs. 5(a) and 6 reveals a difference in energy by 3 orders of magnitude. One should not expect agreement, because the two physical situations are different: single electron vs. an infinite line charge with linear density $\rho = e/\Delta y$. The latter contains an arbitrary parameter Δy , and the final calculated energy W is inversely proportional to this parameter ($W \propto \rho^2 \Delta y = (e/\Delta y)^2 \Delta y = e^2/\Delta y$ – we are grateful to Urs Häusler for pointing this out). For Fig. 6 the parameter Δy was arbitrarily chosen to equal 1 nm (radiation is generated by a line of charge with a transverse charge density of $e/1$ nm; radiation W is collected from a longitudinal strip of the grating of width 1 nm), a length

not connected with the characteristic length scales of the considered grating/beam configuration. It appears reasonable to replace $\Delta y = 1 \text{ nm}$ with $\Delta y = \lambda_{\perp}$, which is one of the characteristic lengths of the system. The result is shown in Table 3. The 2D result now predicts the order of

Geometry of the model	Radiated energy W
3D model	$3.12 \cdot 10^{-25} \text{ J}$
2D model, $\Delta y = \lambda_{\perp} = 914 \text{ nm}$	$2.02 \cdot 10^{-25} \text{ J}$
2D model, $\Delta y = 1 \text{ nm}$	$1.85 \cdot 10^{-22} \text{ J}$

Table 3. Comparison of 3D and 2D SP radiation in the angular range $88.7^{\circ} < \theta < 91.3^{\circ}$ for a metallic grating with beam/grating configuration of Fig. 1.

magnitude of the 3D result. It remains an open question whether this trick would work equally well for other beam/grating configurations.

6. Metallic triangular grating (3D)

In previous sections we considered rectangular gratings. In this section we briefly consider a 3D model of a grating with a triangular profile shown in Fig. 7. This is motivated by the

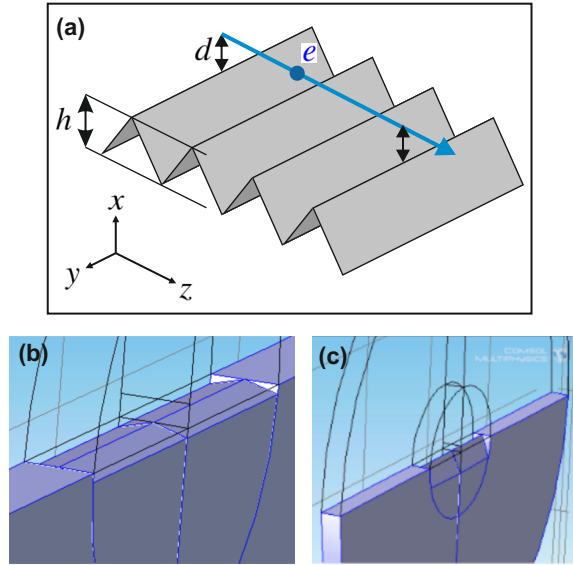


Fig. 7. (a) An infinite triangular grating, 3D model. All parameters are the same as in Fig. 1, but h is varied. (b) The unit cell for $h = 40 \text{ nm}$ and (c) $h = 320 \text{ nm}$. In all cases the grating period and the impact parameter are $a = 300 \text{ nm}$, $d = 100 \text{ nm}$.

expectation that the surface current model of Ref. [28] should work well for such a configuration, provided that the grating is shallow, $h \ll a$, so that resonant cavities do not form. We decided to test this hypothesis. In Table 4 we compare our 3D results with the analytical result based on formulas from Ref. [28]. Similarly as in Fig. 5(a), we obtain an order of magnitude agreement. However, contrary to our expectations, the agreement gets worse as the tooth height is decreased.

Grating tooth height h	W , numerical model	W' , analytical model	Ratio W'/W
40 nm	$1.42 \cdot 10^{-27}$ J	$5.7 \cdot 10^{-27}$ J	4.0
80 nm	$3.18 \cdot 10^{-27}$ J	$1.1 \cdot 10^{-26}$ J	3.5
160 nm	$4.96 \cdot 10^{-27}$ J	$1.2 \cdot 10^{-26}$ J	2.4
320 nm	$6.28 \cdot 10^{-27}$ J	$6.7 \cdot 10^{-27}$ J	1.1

Table 4. SP radiation from metallic triangular gratings, in the angular range $88.7^\circ < \theta < 91.3^\circ$, per electron per grating period, for grating geometry shown in Fig. 7. We compare our numerical results with the analytical model of Ref. [28]

We believe that this points either to the inexactness of surface current model even for shallow gratings, or to some multiplicative factor issue as discussed at the end of Sect. 2.1. This remains an open question, we have only checked that it is not the frequency range issue $(-\infty, \infty)$ vs. $(0, \infty)$, because Eqs (14.60) and (14.70) in Ref. [48], which are the starting point in Ref. [25], are for $\omega \in (0, \infty)$, same as assumed in our calculations.

7. Summary and conclusions

We constructed a numerical frequency-domain model useful for quick calculations of Smith-Purcell radiation intensity from a single particle, verified its accuracy, and discussed some concrete applications. We were somewhat conservative in the choice of grating geometry (rectangular and triangular gratings of uniform material). This was a deliberate choice which facilitated comparison with the older literature. The paper in large part deals with the method, but also presents new results regarding comparison of SP radiation from metallic and dielectric gratings; the possible numerous other applications are left for future work. The main results of the paper can be summarized as follows:

1. A frequency-domain numerical model offers quick calculations of SP radiation intensity (seconds for 2D models, minutes for 3D models, for one frequency, on a single CPU machine).
2. While it is relatively easy to calculate SP radiation in arbitrary units, obtaining an accurate result in concrete units with no spurious multiplicative constants requires careful differentiation between phasors (quantities expected by the numerical solver) and phasor densities (temporal Fourier transforms). After this issue is properly taken care of, the model is simple, easy to implement, and its accuracy is limited only by the spatial mesh density, possibly limited by the amount of RAM computer memory accessible to the user.
3. The accuracy of the numerical model can be conveniently checked against the analytical result: the Frank-Tamm formula.
4. For 30 keV electrons dielectric gratings are less efficient in terms of intensity of SP radiation than their metallic counterpart, by an order of magnitude for silicon, and two orders of magnitude for silica.
5. The described numerical model captures resonant effects in the grating which are not accounted for in some analytical models. In particular, both for metallic and dielectric gratings, SP radiation intensity oscillates with grating tooth height. Both for metals and dielectrics, the optimum tooth height for maximal SP radiation perpendicular to the grating is close to a quarter of the radiation wavelength.

6. For dielectric gratings, more SP radiation enters the grating bulk than is radiated outward into the vacuum.

Funding

This work was supported by the Gordon and Betty Moore Foundation (grant no. GBMF4744) and the U.S. Department of Energy, Office of Science (grant nos. DE-AC02-76SF00515 and DE-SC0009914). LS was supported by the Israel Science Foundation.

Acknowledgments

We are grateful to Avi Gover for pointing us to the older literature on the Smith-Purcell effect and for helpful comments; to Yen-Chieh Huang, Koby Scheuer, Naama Cohen and Urs Häusler for inspiring discussions.

A.S. is grateful to the Wrocław Centre for Networking and Supercomputing for granting access to the Platon U3 computing infrastructure.

Disclosures

The authors declare no conflicts of interest.

A. Energy spectral density – derivation of Eq. (6)

We will show that

$$\int_{-\infty}^{\infty} \mathbf{E}(\mathbf{r}, t) \times \mathbf{H}(\mathbf{r}, t) dt = \int_0^{\infty} 4 \cdot 2\pi \cdot \text{Re} \left[\frac{1}{2} \mathbf{E}(\mathbf{r}, \omega) \times \mathbf{H}^*(\mathbf{r}, \omega) \right] d\omega \quad (13)$$

which is equivalent to Eq. (6). This formula is a version of the Parseval's theorem useful for frequency-domain electromagnetic calculations; it shows the connection between the energy distribution in time and energy distribution in frequency. All equations are consistent with the Fourier transform convention of Eq. (2).

First we determine the Fourier transform of the Poynting vector.

$$\mathbf{S}(\mathbf{r}, t) = \mathbf{E}(\mathbf{r}, t) \times \mathbf{H}(\mathbf{r}, t) = \int_{-\infty}^{\infty} \mathbf{E}(\mathbf{r}, \omega') e^{j\omega' t} d\omega' \times \int_{-\infty}^{\infty} \mathbf{H}(\mathbf{r}, \omega'') e^{j\omega'' t} d\omega'' \quad (14)$$

$$= \int_{-\infty}^{\infty} \int_{-\infty}^{\infty} e^{j(\omega' + \omega'') t} \mathbf{E}(\mathbf{r}, \omega') \times \mathbf{H}(\mathbf{r}, \omega'') d\omega'' d\omega' \quad (15)$$

After the change of variable in the inner integral, $\omega = \omega' + \omega''$, $d\omega = d\omega''$, we obtain

$$\mathbf{S}(\mathbf{r}, t) = \int_{-\infty}^{\infty} \int_{-\infty}^{\infty} e^{j\omega t} \mathbf{E}(\mathbf{r}, \omega') \times \mathbf{H}(\mathbf{r}, \omega - \omega') d\omega d\omega' \quad (16)$$

$$= \int_{-\infty}^{\infty} e^{j\omega t} \underbrace{\int_{-\infty}^{\infty} \mathbf{E}(\mathbf{r}, \omega') \times \mathbf{H}(\mathbf{r}, \omega - \omega') d\omega'}_{\mathbf{S}(\mathbf{r}, \omega)} d\omega \quad (17)$$

This shows that the Fourier transform of the Poynting vector $\mathbf{S}(\mathbf{r}, \omega)$ is the convolution of transforms of the fields (convolution theorem).

From the definition of the Poynting vector and Eq. (17), the total energy radiated through a surface is

$$W = \int_{-\infty}^{\infty} \int_{\text{surface}} \mathbf{S}(\mathbf{r}, t) \cdot d\mathbf{A} dt \quad (18)$$

$$= \int_{-\infty}^{\infty} \int_{\text{surface}} \int_{-\infty}^{\infty} e^{j\omega t} \int_{-\infty}^{\infty} \mathbf{E}(\mathbf{r}, \omega') \times \mathbf{H}(\mathbf{r}, \omega - \omega') d\omega' d\omega \cdot d\mathbf{A} dt \quad (19)$$

Similarly as in Ref. [48], chapter 14.5, we simplify the formula by noting a representation of the delta function, $\int_{-\infty}^{\infty} e^{j\omega t} dt = 2\pi\delta(\omega)$, and noting that $\mathbf{H}(\mathbf{r}, -\omega') = \mathbf{H}^*(\mathbf{r}, \omega')$ (a property of transforms of real functions):

$$W = \int_{\text{surface}} 2\pi \int_{-\infty}^{\infty} \mathbf{E}(\mathbf{r}, \omega') \times \mathbf{H}^*(\mathbf{r}, \omega') d\omega' \cdot d\mathbf{A} \quad (20)$$

In experimental investigations, a useful, measurable quantity is the distribution of energy in positive frequencies, so we reduce the domain of integration over frequencies:

$$W = \int_{\text{surface}} 2\pi \int_0^{\infty} [\mathbf{E}(\mathbf{r}, \omega') \times \mathbf{H}^*(\mathbf{r}, \omega') + \mathbf{E}^*(\mathbf{r}, \omega') \times \mathbf{H}(\mathbf{r}, \omega')] d\omega' \cdot d\mathbf{A} \quad (21)$$

$$= \int_{\text{surface}} 4 \cdot 2\pi \int_0^{\infty} \text{Re} \left[\frac{1}{2} \mathbf{E}(\mathbf{r}, \omega') \times \mathbf{H}^*(\mathbf{r}, \omega') \right] d\omega' \cdot d\mathbf{A} \quad (22)$$

The factor $\frac{1}{2}$ is for easy comparison with the energy formula for phasors (5).

B. Derivation of the Frank-Tamm formula from the potentials

For additional verification of Eq. (6), we will use it to derive the Frank-Tamm formula. The potentials for a point charge ($-e$) moving with velocity βc in a uniform medium characterized by the refractive index n , can be expressed as

$$A_r = 0, A_\phi = 0, A_z(r, z, \omega) = (-e) \frac{\mu_0}{(2\pi)^2} K_0 \left(j \frac{\omega}{c} r \sqrt{n^2 - \beta^2} \right) \exp \left(-j \frac{\omega}{\beta c} z \right), \quad (23)$$

$$\Phi(r, z, \omega) = \frac{c}{n^2 \beta} A_z(r, z, \omega), \quad (24)$$

see Ref. [52], Eqs (2.1.36–38), (2.4.20). K_0 is a modified Bessel function of the second kind. In subsequent calculations, to determine the energy flow in the far field, we use the first term of the asymptotic expansion of K_0 :

$$K_0(j\xi) \simeq \sqrt{\frac{\pi}{2\xi}} e^{-j\pi/4} e^{-j\xi} \quad \text{for } \xi \gg 1 \quad (25)$$

Consider a cylindrical surface of radius r and length Δz surrounding the electron trajectory. According to Eq. (6), the energy radiated through this surface is

$$\Delta W = \int_0^{\infty} \left\{ 4 \cdot 2\pi \cdot (2\pi r \Delta z) \hat{\mathbf{r}} \cdot \text{Re} \left[\frac{1}{2} \mathbf{E}(\mathbf{r}, \omega) \times \frac{1}{\mu_0} \mathbf{B}^*(\mathbf{r}, \omega) \right] \right\} d\omega \quad (26)$$

The fields are determined from the potentials in the usual manner – the equations for transforms are the same as for phasors:

$$\mathbf{E}(\mathbf{r}, \omega) = -j\omega \mathbf{A}(\mathbf{r}, \omega) - \nabla \Phi(\mathbf{r}, \omega) = -j\omega A_z \hat{\mathbf{z}} - \frac{c}{n^2 \beta} \left(\hat{\mathbf{r}} \frac{\partial A_z}{\partial r} + \hat{\mathbf{z}} \frac{\partial A_z}{\partial z} \right) \quad (27)$$

$$\mathbf{B}^*(\mathbf{r}, \omega) = \nabla \times \mathbf{A}^*(\mathbf{r}, \omega) = -\hat{\phi} \frac{\partial A_z^*}{\partial r} \quad (28)$$

Here the scalar potential was eliminated using Eq. (24), and the fields are all expressed as a function of the longitudinal component of the vector potential. Derivatives of A_z are computed using Eqs. (23) and (25). We obtain

$$\hat{\mathbf{r}} \cdot [\mathbf{E}(\mathbf{r}, \omega) \times \mu_0^{-1} \mathbf{B}^*(\mathbf{r}, \omega)] = \mu_0^{-1} \left[-j\omega + \frac{c}{n^2 \beta} \left(j \frac{\omega}{\beta c} \right) \right] A_z \left[-\frac{1}{2r} + j \frac{\omega}{c} \sqrt{n^2 - \beta^2} \right] A_z^* \quad (29)$$

The real part of this expression depends on whether the Cherenkov radiation condition is fulfilled ($\beta c > c/n$):

$$\hat{\mathbf{r}} \cdot \text{Re}[\mathbf{E}(\mathbf{r}, \omega) \times \mu_0^{-1} \mathbf{B}^*(\mathbf{r}, \omega)] = \begin{cases} \omega \left(1 - \frac{1}{n^2 \beta^2}\right) \frac{\mu_0 e^2}{32\pi^3 r} & \text{for } n > 1/\beta \\ 0 & \text{for } n < 1/\beta \end{cases} \quad (30)$$

Insertion of this expression into Eq. (26) yields the energy radiated by the charge per unit travelled length – the Frank–Tamm formula [47–49]:

$$\Delta W / \Delta z = \int_0^\infty \left\{ \begin{array}{ll} e^2 \frac{\mu_0}{4\pi} \omega \left(1 - \frac{1}{n^2 \beta^2}\right) & \text{for } n > 1/\beta \\ 0 & \text{for } n < 1/\beta \end{array} \right\} d\omega. \quad (31)$$

References

1. S. J. Smith and E. M. Purcell, “Visible light from localized surface charges moving across a grating,” *Phys. Rev.* **92**, 1069–1069 (1953).
2. F. Rusin and G. Bogomolov, “Orotron—an electronic oscillator with an open resonator and reflecting grating,” *Proc. IEEE* **57**, 720–722 (1969).
3. Y. A. Grishin, M. R. Fuchs, A. Schnegg, A. A. Dubinskii, B. S. Dumesh, F. S. Rusin, V. L. Bratman, and K. Möbius, “Pulsed orotron—a new microwave source for submillimeter pulse high-field electron paramagnetic resonance spectroscopy,” *Rev. Sci. Instruments* **75**, 2926–2936 (2004).
4. J.-K. So, K. F. MacDonald, and N. I. Zheludev, “Fiber optic probe of free electron evanescent fields in the optical frequency range,” *Appl. Phys. Lett.* **104**, 201101 (2014).
5. Y. Ye, F. Liu, M. Wang, L. Tai, K. Cui, X. Feng, W. Zhang, and Y. Huang, “Deep-ultraviolet Smith–Purcell radiation,” *Optica* **6**, 592 (2019).
6. C. Roques-Carmes, S. E. Kooi, Y. Yang, A. Massuda, P. D. Keathley, A. Zaidi, Y. Yang, J. D. Joannopoulos, K. K. Berggren, I. Kammer, and M. Soljačić, “Towards integrated tunable all-silicon free-electron light sources,” *Nat. Commun.* **10** (2019).
7. R. C. Fernow, “Design of a grating for studying Smith–Purcell radiation and electron acceleration,” in *AIP Conference Proceedings*, (AIP, 1989).
8. G. Doucas, M. Kimmitt, J. Brownell, S. Trotz, and J. Walsh, “A new type of high-resolution position sensor for ultra-relativistic beams,” *Nucl. Instruments Methods Phys. Res. Sect. A: Accel. Spectrometers, Detect. Assoc. Equip.* **474**, 10–18 (2001).
9. K. Soong and R. L. Byer, “Design of a subnanometer resolution beam position monitor for dielectric laser accelerators,” *Opt. Lett.* **37**, 975 (2012).
10. M. Lampel, “Coherent Smith–Purcell radiation as a pulse length diagnostic,” *Nucl. Instruments Methods Phys. Res. Sect. A: Accel. Spectrometers, Detect. Assoc. Equip.* **385**, 19–25 (1997).
11. D. C. Nguyen, “Coherent smith-purcell radiation as a diagnostic for subpicosecond electron bunch length,” *Nucl. Instruments Methods Phys. Res. Sect. A: Accel. Spectrometers, Detect. Assoc. Equip.* **393**, 514–518 (1997).
12. G. Doucas, M. F. Kimmitt, A. Doria, G. P. Gallerano, E. Giovenale, G. Messina, H. L. Andrews, and J. H. Brownell, “Determination of longitudinal bunch shape by means of coherent Smith–Purcell radiation,” *Phys. Rev. Special Top. - Accel. Beams* **5** (2002).
13. V. Blackmore, G. Doucas, C. Perry, B. Ottewell, M. F. Kimmitt, M. Woods, S. Molloy, and R. Arnold, “First measurements of the longitudinal bunch profile of a 28.5 GeV beam using coherent Smith–Purcell radiation,” *Phys. Rev. Special Top. - Accel. Beams* **12** (2009).
14. R. Bartolini, C. Clarke, N. Delerue, G. Doucas, and A. Reichold, “Electron bunch profile reconstruction in the few fs regime using coherent Smith–Purcell radiation,” *J. Instrumentation* **7**, P01009–P01009 (2012).
15. R. J. England, R. J. Noble, K. Bane, D. H. Dowell, C.-K. Ng, J. E. Spencer, S. Tantawi, Z. Wu, R. L. Byer, E. Peralta, K. Soong, C.-M. Chang, B. Montazeri, S. J. Wolf, B. Cowan, J. Dawson, W. Gai, P. Hommelhoff, Y.-C. Huang, C. Jing, C. McGuinness, R. B. Palmer, B. Naranjo, J. Rosenzweig, G. Travish, A. Mizrahi, L. Schachter, C. Sears, G. R. Werner, and R. B. Yoder, “Dielectric laser accelerators,” *Rev. Mod. Phys.* **86**, 1337–1389 (2014).
16. N. V. Sapra, K. Y. Yang, D. Verdecruyse, K. J. Leedle, D. S. Black, R. J. England, L. Su, R. Trivedi, Y. Miao, O. Solgaard, R. L. Byer, and J. Vučković, “On-chip integrated laser-driven particle accelerator,” *Science* **367**, 79–83 (2020).
17. Y. Yang, A. Massuda, C. Roques-Carmes, S. E. Kooi, T. Christensen, S. G. Johnson, J. D. Joannopoulos, O. D. Miller, I. Kammer, and M. Soljačić, “Maximal spontaneous photon emission and energy loss from free electrons,” *Nat. Phys.* **14**, 894–899 (2018).
18. L. G. Sukhikh, G. A. Naumenko, Y. A. Popov, and A. P. Potylitsyn, “Comparison of coherent Smith–Purcell radiation generated by 6.1 MeV electron beam in metal and dielectric lamellar gratings,” (2010).

19. A. P. Potylitsyn, *Smith–Purcell Radiation* (Springer Berlin Heidelberg, Berlin, Heidelberg, 2011), pp. 135–164.
20. D. V. Karlovets and A. P. Potylitsyn, “Comparison of Smith-Purcell radiation models and criteria for their verification,” *Phys. Rev. Special Top. - Accel. Beams* **9** (2006).
21. M. Malovytsia and N. Delerue, “Comparison of the Smith-Purcell Radiation Yield for Different Models,” in *Proc. of International Particle Accelerator Conference (IPAC’16), Busan, Korea, May 8-13, 2016*, (JACoW, Geneva, Switzerland, 2016), no. 7 in International Particle Accelerator Conference, pp. 75–77. Doi:10.18429/JACoW-IPAC2016-MOPMB004.
22. G. T. di Francia, “On the theory of some Čerenkovian effects,” *Il Nuovo Cimento* **16**, 61–77 (1960).
23. C. W. Barnes and K. G. Dedrick, “Radiation by an electron beam interacting with a diffraction grating. two-dimensional theory,” *J. Appl. Phys.* **37**, 411–418 (1966).
24. É. Lalor, “Three-dimensional theory of the Smith—Purcell effect,” *Phys. Rev. A* **7**, 435–446 (1973).
25. J. H. Brownell, J. Walsh, and G. Doucas, “Spontaneous Smith-Purcell radiation described through induced surface currents,” *Phys. Rev. E* **57**, 1075–1080 (1998).
26. S. R. Trotz, J. H. Brownell, J. E. Walsh, and G. Doucas, “Optimization of Smith-Purcell radiation at very high energies,” *Phys. Rev. E* **61**, 7057–7064 (2000).
27. G. Kube, H. Backe, H. Euteneuer, A. Grendel, F. Hagenbuck, H. Hartmann, K. H. Kaiser, W. Lauth, H. Schöpe, G. Wagner, T. Walcher, and M. Kretschmar, “Observation of optical Smith-Purcell radiation at an electron beam energy of 855 MeV,” *Phys. Rev. E* **65** (2002).
28. J. H. Brownell and G. Doucas, “Role of the grating profile in Smith-Purcell radiation at high energies,” *Phys. Rev. Special Top. - Accel. Beams* **8** (2005).
29. P. M. van den Berg, “Smith–Purcell radiation from a line charge moving parallel to a reflection grating,” *J. Opt. Soc. Am.* **63**, 689 (1973).
30. P. M. van den Berg, “Smith–Purcell radiation from a point charge moving parallel to a reflection grating,” *J. Opt. Soc. Am.* **63**, 1588 (1973).
31. P. M. van den Berg and T. H. Tan, “Smith-Purcell radiation from a line charge moving parallel to a reflection grating with rectangular profile,” *J. Opt. Soc. Am.* **64**, 325 (1974).
32. Y. Shibata, S. Hasebe, K. Ishi, S. Ono, M. Ikezawa, T. Nakazato, M. Oyamada, S. Urasawa, T. Takahashi, T. Matsuyama, K. Kobayashi, and Y. Fujita, “Coherent Smith-Purcell radiation in the millimeter-wave region from a short-bunch beam of relativistic electrons,” *Phys. Rev. E* **57**, 1061–1074 (1998).
33. O. Haeberlé, P. Rullhusen, J.-M. Salomé, and N. Maene, “Calculations of Smith-Purcell radiation generated by electrons of 1–100 MeV,” *Phys. Rev. E* **49**, 3340–3352 (1994).
34. Y.-C. Lai, T. C. Kuang, B. H. Cheng, Y.-C. Lan, and D. P. Tsai, “Generation of convergent light beams by using surface plasmon locked Smith-Purcell radiation,” *Sci. Reports* **7** (2017).
35. I. Kaminer, S. Kooi, R. Shiloh, B. Zhen, Y. Shen, J. López, R. Remez, S. Skirlo, Y. Yang, J. Joannopoulos, A. Arie, and M. Soljačić, “Spectrally and spatially resolved Smith-Purcell radiation in plasmonic crystals with short-range disorder,” *Phys. Rev. X* **7** (2017).
36. R. Remez, N. Shapira, C. Roques-Carmes, R. Tirole, Y. Yang, Y. Lereah, M. Soljačić, I. Kaminer, and A. Arie, “Spectral and spatial shaping of Smith-Purcell radiation,” *Phys. Rev. A* **96** (2017).
37. A. Massuda, C. Roques-Carmes, Y. Yang, S. E. Kooi, Y. Yang, C. Murdia, K. K. Berggren, I. Kaminer, and M. Soljačić, “Smith–Purcell radiation from low-energy electrons,” *ACS Photonics* **5**, 3513–3518 (2018).
38. W. Liu and Z. Xu, “Special Smith–Purcell radiation from an open resonator array,” *New J. Phys.* **16**, 073006 (2014).
39. K. Lekontsev, P. Karataev, A. Tishchenko, and J. Urakawa, “CST simulations of THz Smith–Purcell radiation from a lamellar grating with vacuum gaps,” *Nucl. Instruments Methods Phys. Res. Sect. B: Beam Interactions with Mater. Atoms* **355**, 164–169 (2015).
40. A. Aryshev, A. Potylitsyn, G. Naumenko, M. Shevelev, K. Lekontsev, L. Sukhikh, P. Karataev, Y. Honda, N. Terunuma, and J. Urakawa, “Monochromaticity of coherent Smith-Purcell radiation from finite size grating,” *Phys. Rev. Accel. Beams* **20** (2017).
41. H. Zhang, I. Konoplev, and G. Doucas, “A coherent Smith-Purcell radiation source: design considerations for a high power, tunable source of terahertz radiation,” in *2019 44th International Conference on Infrared, Millimeter, and Terahertz Waves (IRMMW-THz)*, (IEEE, 2019).
42. Y. Song, J. Du, N. Jiang, L. Liu, and X. Hu, “Efficient terahertz and infrared Smith–Purcell radiation from metal-slot metasurfaces,” *Opt. Lett.* **43**, 3858 (2018).
43. A. Tyukhtin, V. Vorobev, E. Belonogaya, and S. Galyamin, “Radiation of a charge in presence of a dielectric object: aperture method,” *J. Instrumentation* **13**, C02033–C02033 (2018).
44. S. Galyamin, A. Tyukhtin, and V. Vorobev, “Focusing the cherenkov radiation using dielectric concentrator: simulations and comparison with theory,” *J. Instrumentation* **13**, C02029–C02029 (2018).
45. S. N. Galyamin, V. V. Vorobev, and A. Benediktovitch, “Radiation field of an ideal thin gaussian bunch moving in a periodic conducting wire structure,” *Phys. Rev. Accel. Beams* **22** (2019).
46. “Comsol Multiphysics, version 4.3,” <https://www.comsol.com>.
47. I. Frank and I. Tamm, “Coherent visible radiation of fast electrons passing through matter,” *Comptes rendus de l’Académie des sciences de l’URSS* **14**, 109–114 (1937).
48. J. D. Jackson, *Classical Electrodynamics* (Wiley, 1998), 3rd ed.
49. T. Shiozawa, *Classical Relativistic Electrodynamics* (Springer Berlin Heidelberg, 2004).

50. W. Liu, W. Li, Z. He, and Q. Jia, "Theory of the special Smith-Purcell radiation from a rectangular grating," *AIP Adv.* **5**, 127135 (2015).
51. H. Haus, *Waves and fields in optoelectronics* (Prentice Hall, Incorporated, 1984).
52. L. Schächter, *Beam-Wave Interaction in Periodic and Quasi-Periodic Structures* (Springer Berlin Heidelberg, 2011).
53. S. L. Chuang and J. A. Kong, "Enhancement of Smith-Purcell radiation from a grating with surface-plasmon excitation," *J. Opt. Soc. Am. A* **1**, 672 (1984).
54. Y. Pan and A. Gover, "Spontaneous and stimulated radiative emission of modulated free-electron quantum wavepackets—semiclassical analysis," *J. Phys. Commun.* **2**, 115026 (2018).
55. A. Szczepkowicz, "Numerical calculation of the Smith-Purcell radiation from dielectric laser acceleration (DLA) structures," <https://agenda.infn.it/event/17304/contributions/98899/> (2019). Poster presented at the European Advanced Accelerator Concepts Workshop (EAAC2019), Elba, Italy.
56. A. Szczepkowicz, "Guided-mode resonance, resonant grating thickness, and finite-size effects in dielectric laser acceleration structures," *Appl. Opt.* **55**, 2634 (2016).
57. U. Häusler *et al.* In preparation.
58. K. M. McPeak, S. V. Jayanti, S. J. P. Kress, S. Meyer, S. Iotti, A. Rossinelli, and D. J. Norris, "Plasmonic films can easily be better: Rules and recipes," *ACS Photonics* **2**, 326–333 (2015). PMID: 25950012.
59. M. Polyanskiy, "Refractive index database," <https://refractiveindex.info/> (2020).
60. I. H. Malitson, "Interspecimen comparison of the refractive index of fused silica," *J. Opt. Soc. Am.* **55**, 1205 (1965).
61. C. Schinke, P. C. Peest, J. Schmidt, R. Brendel, K. Bothe, M. R. Vogt, I. Kröger, S. Winter, A. Schirmacher, S. Lim, H. T. Nguyen, and D. MacDonald, "Uncertainty analysis for the coefficient of band-to-band absorption of crystalline silicon," *AIP Adv.* **5**, 067168 (2015).
62. P. Yousefi, N. Schönenberger, J. Mcneur, M. Kozák, U. Niedermayer, and P. Hommelhoff, "Dielectric laser electron acceleration in a dual pillar grating with a distributed bragg reflector," *Opt. Lett.* **44**, 1520 (2019).
63. A. P. Potylitsyn, M. I. Ryazanov, M. N. Strikhanov, and A. A. Tishchenko, *Diffraction Radiation from Relativistic Particles* (Springer Berlin Heidelberg, 2011).
64. A. I. Nosich, "Diffraction radiation which accompanies the motion of charged particles near an open resonator," *Radiophys. Quantum Electron.* **24**, 696–701 (1981).
65. D. O. Yevtushenko, S. V. Dukhopelnykov, and A. I. Nosich, "Optical diffraction radiation from a dielectric and a metal nanowire excited by a modulated electron beam," *Opt. Quantum Electron.* **51** (2019).
66. É. I. Veliev, A. I. Nosich, and V. P. Shestopalov, "Radiation of an electron flux moving over a grating consisting of cylinders with longitudinal slits," *Radiophys. Quantum Electron.* **20**, 306–313 (1977).